Ultrasound in Med. & Biol., Vol. 00, No. 00, pp. 1–13, 2019

0301-5629/$ - see front matter

https://doi.org/10.1016/j.ultrasmedbio.2019.11.020

● *Original Contribution*

4-D ECHO-PARTICLE IMAGE VELOCIMETRY IN A LEFT VENTRICULAR PHANTOM

Jason Voorneveld,* Hicham Saaid,† Christiaan Schinkel,‡ Nikola Radeljic,§ Boris Lippe,§ Frank J.H. Gijsen,* Antonius F.W. van der Steen,*,‖ Nico de Jong,*,‖ Tom Claessens,¶ Hendrik J. Vos,*,‖ Sasa Kenjeres,‡ and Johan G. Bosch*

* Department of Biomedical Engineering, Thorax Center, Erasmus MC University Medical Center, Rotterdam, the Netherlands; † Institute Biomedical Technology, Ghent University, Ghent, Belgium; ‡ Transport Phenomena Section, Department of Chemical Engineering, Faculty of Applied Sciences, Delft University of Technology; the Netherlands; § Oldelft Ultrasound, Delft, the Netherlands; ‖ Laboratory of Acoustical Wavefield Imaging, Faculty of Applied Sciences, Delft University of Technology, Delft, the Netherlands; and ¶ Department of Materials, Textiles and Chemical Engineering, Ghent University, Ghent, Belgium

(*Received* 15 *March* 2019; *revised* 29 *October* 2019; *in final from* 30 *November* 2019)

Abstract—Left ventricular (LV) blood flow is an inherently complex time-varying 3-D phenomenon, where 2-D quantification often ignores the effect of out-of-plane motion. In this study, we describe high frame rate 4-D echocardiographic particle image velocimetry (echo-PIV) using a prototype matrix transesophageal transducer and a dynamic LV phantom for testing the accuracy of echo-PIV in the presence of complex flow patterns. Optical time-resolved tomographic PIV (tomo-PIV) was used as a reference standard for comparison. Echo-PIV and tomo-PIV agreed on the general profile of the LV flow patterns, but echo-PIV smoothed out the smaller flow structures. Echo-PIV also underestimated the flow rates at greater imaging depths, where the PIV kernel size and transducer point spread function were large relative to the velocity gradients. We demonstrate that 4-D echo-PIV could be performed in just four heart cycles, which would require only a short breath-hold, providing promising results. However, methods for resolving high velocity gradients in regions of poor spatial resolution are required before clinical translation. (E-mail: j.voorneveld@erasmusmc.nl) © 2019 The Author(s). Published by Elsevier Inc. on behalf of World Federation for Ultrasound in Medicine & Biology. This is an open access article under the CC BY-NC-ND license. (http://creativecommons.org/licenses/by-nc-nd/4.0/).

Key Words: **High frame rate ultrasound, Ultrafast ultrasound, Ultrasound image velocimetry, Echo particle image velocimetry, Left ventricle, 4-D ultrasound, 4-D echo-PIV, Tomographic PIV, Volumetric flow, Vector flow imaging.**

INTRODUCTION

Blood flow patterns in the left ventricle (LV) are of increasing interest in the study and early diagnosis of LV dysfunction, with particular focus on the transmitral jet and the intra-ventricular vortex dynamics that occur between filling and ejection (Kheradvar et al. 2012; Sengupta et al. 2012b; Martínez-Legazpi et al. 2014; Pasipoularides 2015; Pedrizzetti et al. 2015; Arvidsson et al. 2016). Currently, the primary *in vivo* techniques used for studying LV flow dynamics are phase-contrast magnetic resonance imaging (PC-MRI) and echocardiography.

PC-MRI has the advantage of being able to measure flow patterns in 3-D (often called 4-D flow magnetic resonance imaging [MRI]) and not requiring contrast agent injection, but requires long acquisition times (averaging over hundreds of cardiac cycles), expensive infrastructure and equipment and suffers low temporal resolution (only acquiring 20–30 phases per cardiac cycle) (Dyverfeldt et al. 2015).

Alternatively, clinically available echocardiographic blood flow imaging techniques are bedside-available and can be acquired at 15–100 frames per second, but are currently limited in the flow components that can be measured. Pulsed-wave Doppler can accurately measure blood velocities, but only the velocity component parallel to the ultrasound beam (axial) and in a small interrogation region at a time. Alternatively, color Doppler can visualize blood flow over a region in 2-D, but again only the axial velocity component. Also, aliasing is common when high velocities are present,

Address correspondence to: Jason Voorneveld, Department of Biomedical Engineering, Thorax Center, Erasmus MC University Medical Center, EE 2302, Wytemaweg 80, 3015 CN, Rotterdam, the Netherlands. E-mail: j.voorneveld@erasmusmc.nl

although methods have been proposed to circumvent this issue (Lai et al. 1997; Muth et al. 2011; Posada et al. 2016). Because LV blood flow patterns are inherently 4-D (time-varying 3-D), echocardiographic techniques that can estimate 4-D blood flow patterns, resolving all three spatial components, are required.

Some experimental ultrasound techniques have emerged to address the need for 4-D blood flow measurement. For instance, *vector Doppler* estimates the lateral velocity components by using multiple angled Doppler acquisitions (Correia et al. 2016). Similarly, *transverse oscillation* estimates lateral displacement by introducing a lateral modulation into the received signal (Holbek et al. 2017a; Holbek et al. 2017b). However, transverse oscillation and vector Doppler require larger apertures for greater depths of interest, which is difficult with cardiac imaging owing to the small intercostal windows available. Along similar lines to vector Doppler, Gomez et al. (2015) reconstructed the cycle-averaged blood flow in the LV by combining multiple 3-D Doppler acquisitions from different views and regularizing the result with segmented 3-D wall motion. However, the results required manual dealiasing and alignment of the Doppler data.

Alternatively, *vector flow mapping* calculates lateral velocity components from color Doppler acquisitions and segmentations of the LV wall using a model-based approach (Garcia et al. 2010; Assi et al. 2017). Grønli et al. (2018) expanded this method to adults with the addition of a hybrid blood-speckle tracking and Doppler estimator to circumvent aliasing. However, Grønli et al. (2018) state in the same work that the effect of measurement precision of boundary conditions should be investigated further and the technique should undergo thorough *in vivo* validation.

Blood-speckle tracking estimates the displacement of blood-speckle patterns (Fadnes et al. 2017). For the blood velocities expected in the LV (~1 m/s, higher for regurgitation jets), very high frame rates (HFRs) are required to limit the inter-frame speckle displacement so that tracking is still possible. Wigen et al. (2018) demonstrated 3-D blood speckle tracking in healthy volunteers, using multi-beat (seven heartbeats in total) 3-D volumes and multi-beat 10° wide "thin-slice" acquisitions. Both methods compared well with PC-MRI but mentioned signal-to-noise ratio (SNR) and clutter as significant challenges going forward. Here ultrasound contrast agents (UCAs) microbubbles are useful as they provide large SNR improvements over native blood backscatter. The tracking of microbubbles instead of native blood speckle is called echo-particle image velocimetry (echo-PIV).

Like speckle tracking, echo-PIV also requires HFR echocardiography to accurately track the high velocities present in the LV (Kheradvar et al. 2010; Gao et al. 2013; Gao et al. 2015). HFR echo-PIV has been shown to accurately estimate the high velocities present in the LV *in vitro* (Voorneveld et al. 2018b) and has been demonstrated in humans in 2-D (Toulemonde et al. 2018; Voorneveld et al. 2019).

Some techniques have been proposed for extending echo-PIV to 3-D while still using 1-D array transducers: sweeping/moving the transducer to obtain multiple 2-D echo-PIV fields so that a 3-D field can be reconstructed (Zhou et al. 2019a; Zhou et al. 2019b), using bi-plane acquisitions to estimate velocity fields in two orthogonal directions (Sengupta et al. 2012a), utilizing speckle decorrelation combined with knowledge of the elevational beam profile to estimate out-of-plane motion (Poelma et al. 2011; Zhou et al. 2018; Zhou et al. 2019c). Alternatively, using a matrix transducer in a simulation study, Gao et al. (2013) used multi-line acquisition (frame rate = 113 Hz) to measure blood flow in a simulated LV, but found that the frame rate was too low to measure the high velocities associated with filling and ejection.

Here we investigate the capabilities of a prototype matrix transesophageal (TEE) probe that employs micro-beamforming to reduce the number of channels requiring direct connections to the ultrasound system. The architecture of the probe permits volumetric imaging in a 20° × 20° field of view at the pulse repetition frequency (PRF, 4 kHz in this study). To image the whole LV (60° × 60°), a multi-beat acquisition scheme of just four cycles was used with four beams per cycle, allowing for a frame rate of 1 kHz. The presented technique would allow for 4-D flow-pattern estimation over the whole LV in just four heart beats. The accuracy of HFR echo-PIV using this acquisition scheme is assessed by comparison with time-resolved tomographic PIV (tomo-PIV). Tomo-PIV provides high spatial and temporal resolution 4-D velocity data in a single cycle but requires optical access. For this purpose, we have designed a dynamic LV phantom that can be imaged with both echo-PIV and tomo-PIV. In this study, we assess the accuracy of 4-D echo-PIV when using this prototype matrix TEE probe.

METHODS

LV phantom

A detailed explanation of the LV phantom used in this study is provided in Saaid et al. (2019), but a brief overview will be provided here. An optically and acoustically transparent silicone LV shell (~0.5 mm thick) was modeled on the mean shape of a set of 150 computed tomography patient LV segmentations (Kirişli et al. 2010; Metz et al. 2012). The LV was fitted with bio-prosthetic mitral (25 mm, Perimount, Edwards Lifesciences Corp., Irvine, CA, USA) and aortic (19 mm, Perimount Magna Ease, Edwards Lifesciences Corp.) valves and contained in a rigid acrylic pressure chamber

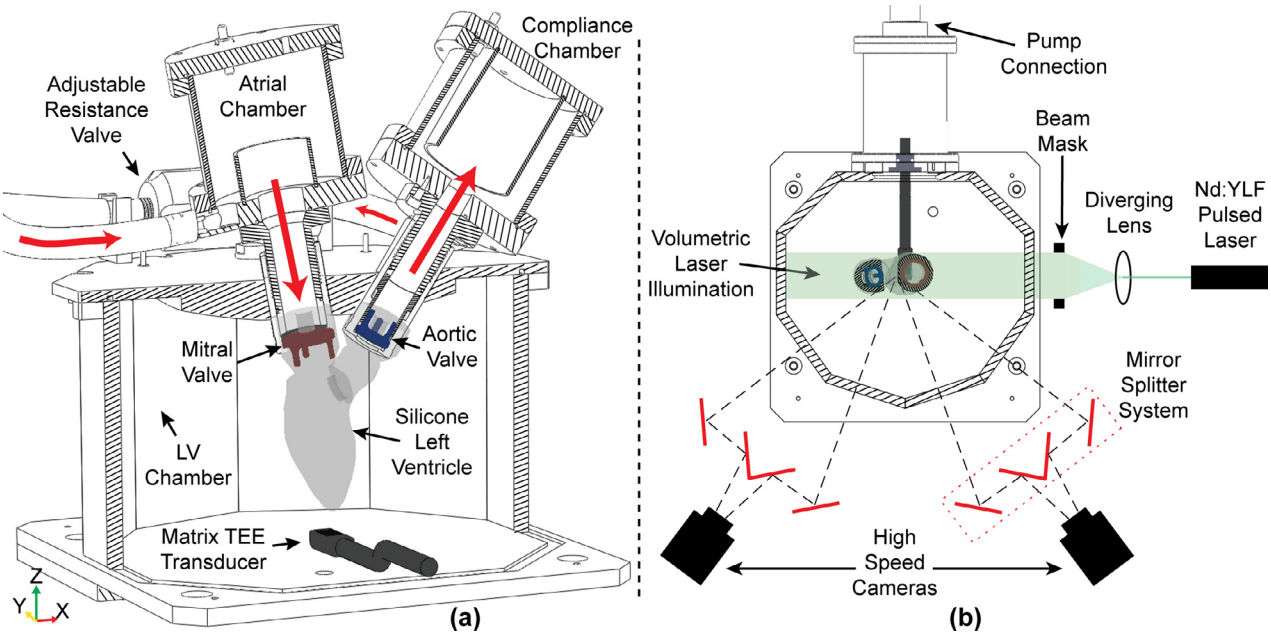

Fig. 1. (a) Partial section view of LV phantom with the matrix TEE transducer shown in its approximate location. Bioprosthetic mitral (red) and aortic (blue) valves are shown in their position. Red arrows indicate direction of flow circuit. Atrial and compliance chambers are connected by a tube with an adjustable resistance valve. (b) Schematic top view of LV phantom showing tomoPIV setup; see text for details. LV = left ventricular; TEE = transesophageal; tomo-PIV = tomographic particle image velocimetry.

with nine faces to allow for optical access (excluding lid and base) (see Fig. 1a). The mitral and aortic tracts of the LV were connected to atrial and compliance chambers (transparent acrylic, built in-house), which were connected *via* a tube with an adjustable resistance valve (ViVitro Labs Inc., Victoria, BC, Canada), forming the LV flow circuit. The rigid pressure chamber was connected to a programmable piston pump (SuperPump, ViVitro Labs Inc.), forming the hydraulic circuit. The hydraulic circuit varied the volume in the rigid chamber, causing the ventricle to expand and contract, pumping fluid through the flow circuit. Both the hydraulic and LV flow circuit were filled with a glycerol in water mixture (60:40 by volume, density = 1160 kg/m^3, dynamic viscosity = 17.7 mPa·s, sound speed = 1790 m/s) to match the refractive index of the silicone LV (1.413). The piston pump oscillated in a sinusoidal pattern (70 beats per min, 50 mL stroke volume), causing the LV to pump the fluid through the flow circuit (red arrows—Fig. 1a). The pump provided an electronic trigger signal for synchronizing acquisitions to a specific phase of the cycle.

Tomo-PIV

A brief overview of the tomo-PIV setup is provided here; for a detailed description, see Saaid et al. (2019). Two high-speed CMOS cameras (Imager Pro HS 4 M, PCO, Kelheim, Germany), recording at 2000 frames per second, were placed behind two sets of custom-built image mirror-splitter systems, to effectively create four independent views of the LV (Fig. 1b). The whole LV volume was then illuminated using a pulsed Nd:YLF laser (527 nm, Litron Laser, Warwickshire, England) passing through a diverging lens system (Fig. 1b) pulsing at 2 kHz (synchronized with the cameras). Fluorescent rhodamine-B-coated particles (diameter = 20−50 μm, density = 1100 kg/m^3) were used as tracer particles and long-pass 540 nm filters (Thorlabs Inc., Newton, NJ, USA) were used to selectively capture the fluorescent signals from the particles. A single pump cycle was captured (857 ms) and processed with Davis 10 software (LaVision, Göttingen, Germany). An iterative window refinement scheme was used, starting with a kernel size of 7.84^3 mm^3 for two iterations, reducing to 5.23^3 mm^3 and finally 3.84^3 mm^3, all with an overlap of 75%. The final spatial grid resolution was 0.96^3 mm^3 and the temporal resolution was 0.5 ms. The measured point spread function (PSF) of a single tracer particle was ~0.3 mm isotropic. Note that no ultrasound was performed for the experiment described by Saaid et al. (2019), and a time-resolved tomo-PIV analysis was performed in this study instead of the phase-averaged study by Saaid et al. (2019).

Ultrasound

A prototype matrix TEE probe (Oldelft, Delft, the Netherlands) was used for imaging (central frequency 5 MHz). It had separated transmit (128 elements, 5.76 × 0.9

mm^2) and received (2048 elements, 8.7×8.7 mm^2) apertures of piezoelectric elements mounted on top of a front-end application-specific integrated circuit (ASIC). The receive aperture was grouped into 128 groups of 4×4 elements, where micro-beamforming was performed on the ASIC for each group, thereby reducing the channel count to 128 in receive (Fig. 2a). A detailed explanation of the probe is provided by Bera et al. (2018). The reduced channel count allowed for the probe to be used with a single Vantage 256 ultrasound system (Verasonics Inc., Kirkland, WA, USA). The probe was positioned below the ventricle, typical of an apical view. The probe was placed approximately 5 mm below and 10 mm septal of the ventricle's apex, inside the rigid pressure chamber and in contact with the hydraulic fluid (see Fig. 1a).

A maximum beam width of $20^\circ \times 20^\circ$ was possible that suppressed grating lobes in receive to −20 dB (which appeared diagonally at 21° from the main lobe owing to the slanted receive aperture). However, this was not sufficient for imaging the full LV volume (Fig. 2b). Thus, to cover the whole LV ($60^\circ \times 60^\circ$), a rectangular grid of four beam steering angles was used in both the elevational and azimuthal directions (−20°, −5°, 5° and 20°) resulting in $4 \times 4 = 16$ beam angles (Fig. 3). An additional constraint was that a PRF limit of 4 kHz to prevent reflection artifacts occurring at higher PRFs (from the LV chamber lid—despite the use of acoustic dampening material on the inside of the lid). Consequently, the use of 16 sequential beams would have resulted in a frame rate of 250 Hz which was not sufficient for high-velocity particle tracking. Therefore, we used a gated sequence of four beams per pump cycle over four cycles to adequately sample the spatial field of view required, while maintaining a frame rate of 1 kHz (see Fig. 3). Note that this gated sequence is not suited for B-mode imaging of the bubbles as their position is not cyclical. However, for velocity mapping, this scheme is acceptable in the case that flow patterns are repeated in each cycle and that cycle periods are consistent, so that the motion of the bubbles is cyclical. In the case of this experiment, these assumptions were reasonable.

It was our intention to use diluted UCA as ultrasound tracer particles. However, the operation of the phantom setup spontaneously generated small air bubbles in the flow circuit with sizes expected to be between 10 and 100 μm which already provided an acceptable concentration of tracer particles. Therefore, no UCA was added.

A diverging wave transmission was performed using a three cycle, 5 MHz tone burst with a PRF of 4 kHz. Peak-negative pressure was measured to be between 260 kPa at 20 mm depth from the probe and 60 kPa at 80 mm depth. Details of the transmit and receive scheme are provided in Table 1.

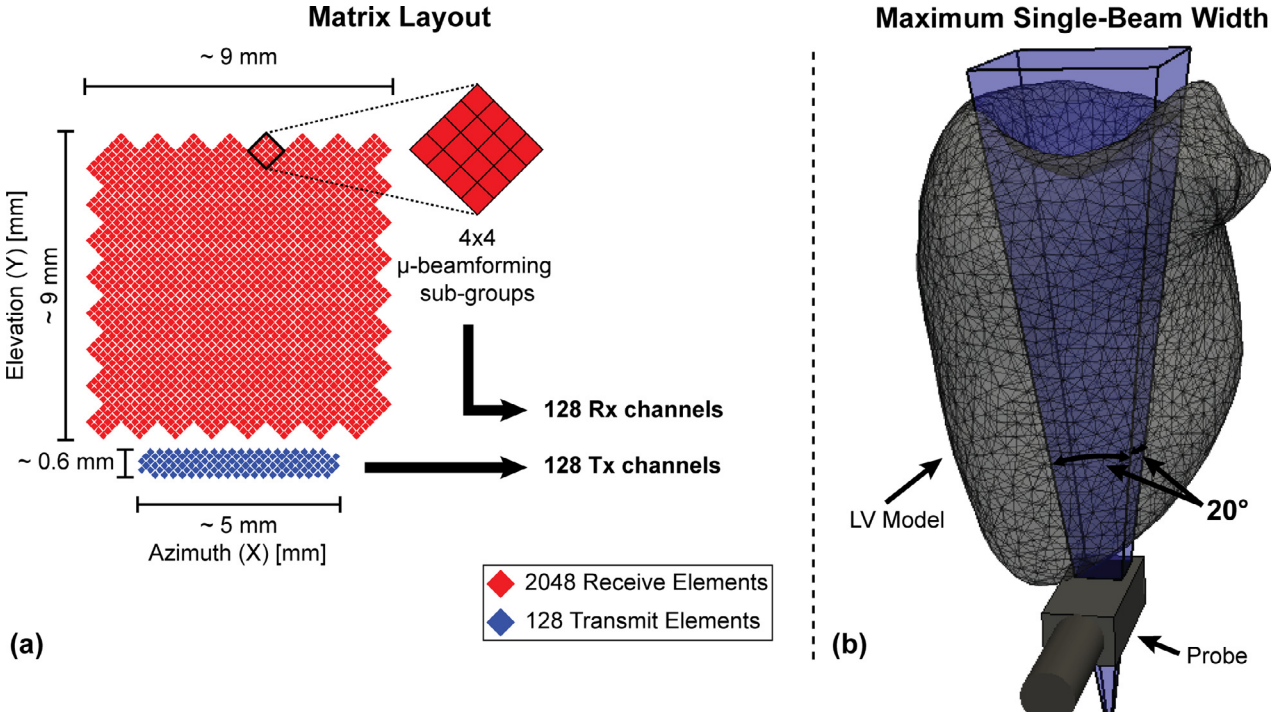

Fig. 2. (a) Schematic layout of matrix elements; note the separated Tx and Rx apertures. The channel requirements in receive are reduced from 2048 to 128 by micro-beamforming in local 4×4 subarrays. (b) The probe architecture imposes a maximum single-beam opening angle of $20^\circ \times 20^\circ$ in receive. This is insufficient to image the entire LV, thus multiple steered beams are required to image the required field of view. Tx = transmit; Rx = receive; LV = left ventricular.

Cycle	Azimuthal Steering (X)	Elevational Steering (Y)
1	-20°, -5°	-20°, -5°
2	5°, 20°	-20°, -5°
3	-20°, -5°	5°, 20°
4	5°, 20°	5°, 20°

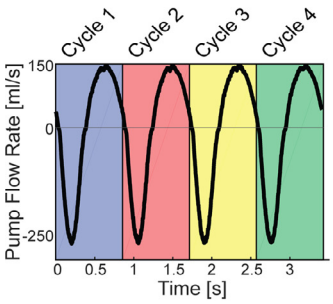

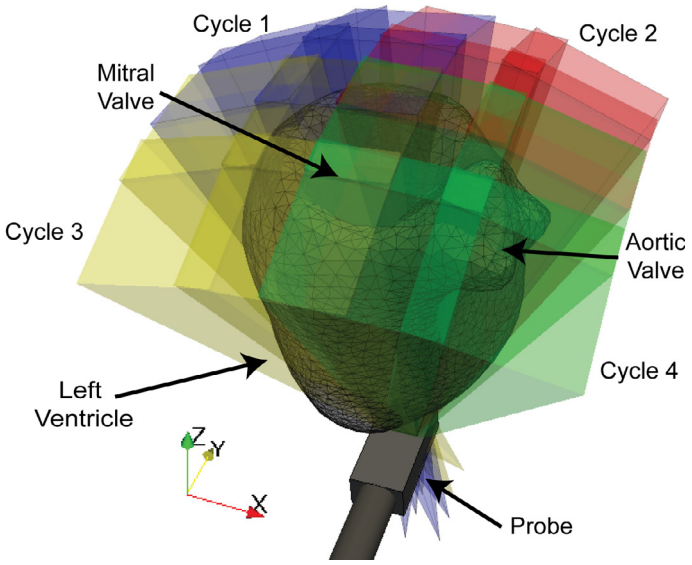

Fig. 3. Spatial sampling of the full LV volume is gated over four pump cycles, with four different beams being acquired successively each cycle (16 total). Thus, a region of 60˚ × 60˚ can be sampled while maintaining a frame rate of 1 kHz, but requiring four cycles to acquire. LV = left ventricular.

Table 1. Ultrasound parameters

Transmit	
Center frequency	5 MHz
Pulse repetition frequency	4 kHz
Virtual focus depth	−21 mm
Apodization	Rectangular
Receive	
Field of view (per beam)	120 mm × 20˚ × 20˚
Field of view (total)	120 mm × 60˚ × 60˚
Apodization	Rectangular
Sample spacing	180 μm × 0.6˚ × 0.6˚
Number of gated cycles	4
Frame rate (per cycle)	1 kHz

Table 2. Echo-PIV parameters

Echo-PIV	
Clutter filter	55 Hz high pass eighth order Butterworth
Similarity metric	Normalized cross-correlation (FFT)
Kernel size	6 mm × 5˚ × 5˚
Iterations	4
Window deformation	Bicubic interpolation
Overlap	50% × 75% × 75%
Particles	10−100 μm air bubbles
Final grid (spherical)	3 mm × 1.25˚ × 1.25˚
Final grid (cartesian)	3 × 1.4 × 1.4 mm^3
Correlation averages	5 frames (5 ms)
Vector frame rate	200 Hz
Subpixel estimator	3 × 1-D Gaussian peak fit
Regularization	
Outlier detection	Universal outlier detector (Westerweel and Scarano 2005)
Gaussian temporal moving average	Standard dev. (σ) = 5 ms Truncation = 3 σ
Gaussian spatial convolution	σ = 1.6 × 0.9 × 0.9 mm^3 Truncation = 1.6 σ

echo-PIV = echocardiographic particle image velocimetry.

Beamforming and echoPIV

Acquired radio frequency (RF) data were first clutter filtered (see Table 2) and then beamformed using Verasonics software (v3.0.10, Verasonics Inc., Kirkland, WA, USA) in Cartesian coordinate space and envelope detected before inverse-scan conversion to a spherical coordinate space. The conversion to spherical space was performed to keep the PSF consistent over depth (see Fig. 4). The speed of sound (1790 m/s) of the phantom fluid was adjusted on the Verasonics software for delay computation in both transmit and receive.

Custom PIV software written in Python (v3.6, Python Software Foundation, Delaware, USA) was used to perform PIV analysis (see Table 2 and Fig. 5) between successive acquisitions with the same beam angle. Ensemble averaging of five successive correlation volumes (averaging of the 3-D normalized cross-correlation functions for successive frames) was used, producing a vector frame rate of 200 Hz. An iterative window deformation algorithm was used where the second image volume was iteratively deformed using the previous iterations displacement estimates as a deformation field (Scarano and Riethmuller 2000). Before echo-PIV analysis, the tomo-PIV data were used to derive a static mask of the LV. For each beam, this mask defined where displacement estimation should be performed. After displacements had been estimated for all 16 beams, they were

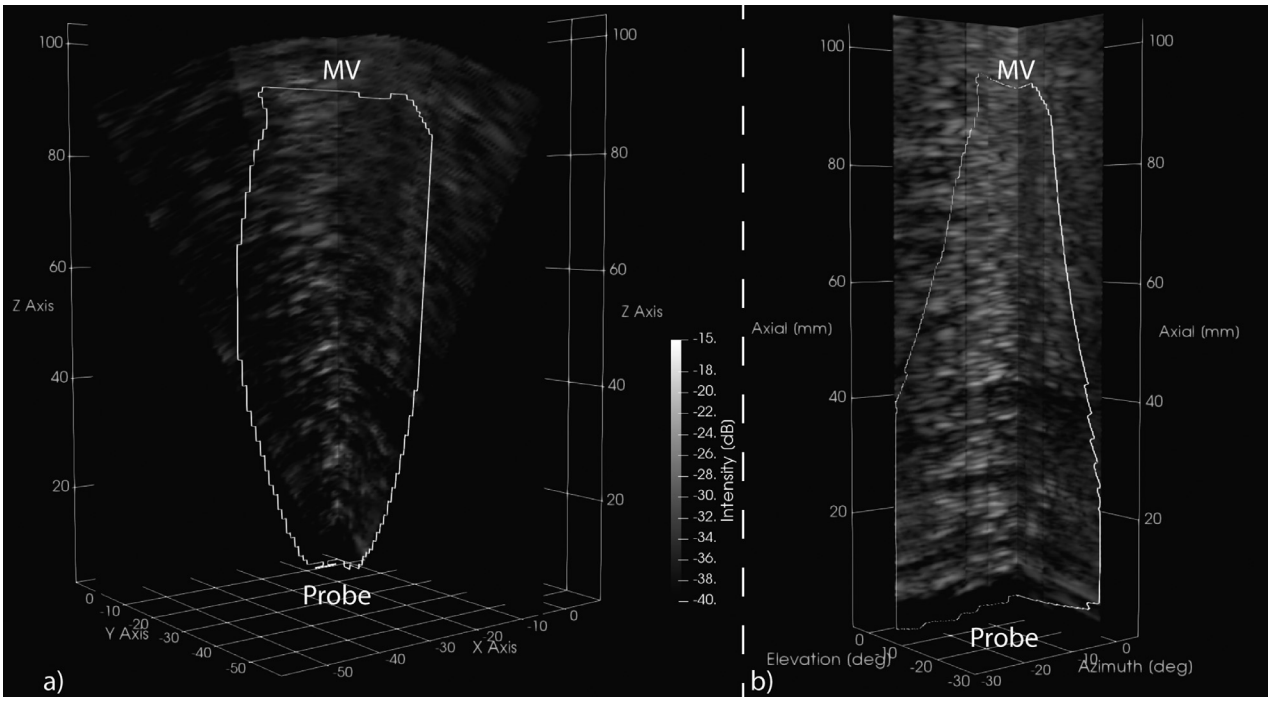

Fig. 4. Cross-plane B-mode images of a single sequential set of four beams (out of four beam groups). The left image (a) is displayed in the Cartesian coordinate system with the approximate LV cavity borders marked with a white line. Right image (b) shows the same time frame in the spherical coordinate system with the spherically converted LV cavity borders shown. Note how the PSF increases with depth for the Cartesian image (a) but stays approximately constant with depth in the spherical coordinate system (b). Also note that the number of voxels describing the MV region in the spherical coordinate system is greatly reduced compared with the Cartesian image. (Video S1, available online). LV = left ventricular; PSF = point spread function; MV = mitral valve.

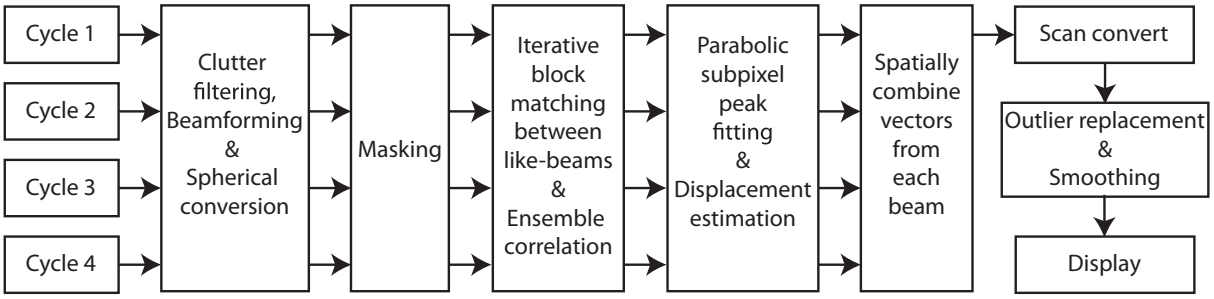

Fig. 5. High-level processing chain utilized in this study. The four sets of beams acquired in each cycle are processed individually and combined spatially and scan converted before outlier replacement and smoothing.

combined, averaging overlapping vectors where applicable. Vector data were then scan converted onto a regular Cartesian grid, using the grid spacing at 50 mm depth as the cross-beam grid spacing (~1.4 mm). Finally, outlier removal and replacement were performed and vectors were regularized on the Cartesian grid using separate temporal and spatial Gaussian convolution filters.

Visualization and comparison

Vector comparison. Vector data were visualized and flow rates computed using Paraview (v5.6, Kitware Inc., New York, USA) (Ahrens et al. 2005). Before comparison the tomo-PIV data were down-sampled to match the grid spacing of the echo-PIV data using a local mean both spatially and temporally. Flow rate through three XY planes (25, 50 and 75 mm deep from the probe) as well as a plane intersecting the outflow tract were computed and compared for both echo-PIV and tomo-PIV. The average velocity magnitude in a 4 mm section in center of the jet (at the same plane depths as the flow calculations) was computed too.

SNR. To estimate the noise reference signal, a no-transmit acquisition was recorded with all other receive

parameters held constant. The SNR could then be calculated using the formula: $= 20\log_{10}(A_{\text{transmit}}/A_{\text{no\_transmit}})$, where A_{transmit} and $A_{\text{no\_transmit}}$ are the average signal amplitudes for recordings with transmit on and off, respectively.

Point spread function. PSF was measured at different depths by measuring the full-width-half-maximum envelope signals of isolated bubbles along the three Cartesian axes.

RESULTS

Description of flow field

Shortly after mitral valve opening, a high-velocity jet forms which is angled toward the septal LV wall (Fig. 6b and 6j). Initially, a vortex ring develops at the head of the jet but the septal side of the ring is diminished when it collides with the septal wall (Fig. 6d). From this moment the posterior side of the vortex ring expands, redirecting flow along the posterior-inferior side of the LV toward the base (Fig. 6d and 6l). Once the mitral valve closes, the fluid swirls in a general clockwise manner along both the azimuthal and elevational (X and Y) axes, with many smaller vortices appearing along the jet's primary flow path (Fig. 6f and 6n). Once the aortic valve opens, flow travels upward along the posterior-inferior wall of the LV and up along the base, passing under the mitral valve, before exiting the LV through the outflow tract in a helical pattern (with higher velocities at the top of the outflow tract than at the bottom) (Fig. 6h).

Qualitative comparison

During the initial stages of filling, when the jet is beginning to form, echo-PIV grossly underestimates the velocity and volume of the jet (Fig. 6a vs. 6b and Fig. 6i vs. 6j). Once the jet has progressed deeper into the LV (closer to the probe), echo-PIV estimates similar velocity magnitudes to tomo-PIV but still estimates the jet to be thinner in volume (Fig. 6c vs. 6d and Fig. 6k vs. 6l). Also, during this phase, echo-PIV and tomo-PIV observe similar shapes and positions of the vortex rings, but the magnitudes are larger in tomo-PIV. During diastasis, echo-PIV and tomo-PIV agree in the general swirling of the flow but a more detailed (winding) flow pattern is observed in the tomo-PIV (Fig. 6e vs. 6f and Fig. 6m vs. 6n). During ejection, echo-PIV observes similar flow to the tomo-PIV, moving up the posterior wall turning to travel along the base, but no ejection is detected in the region of the outflow tract.

Quantitative comparison

Volume flow rate. To quantitatively assess the accuracy of echo-PIV, we calculated the flow rate through various planes (Fig. 7a), including flow through the aortic outflow tract (Fig. 7c), filling flow rates (only flow with negative Z velocity components) calculated through horizontal (XY) planes at depths of 25 mm (Fig. 7d), 50 mm (Fig. 7e) and 75 mm (Fig. 7f) from the probe.

Echo-PIV severely underestimates the flow rate through the outflow tract during ejection (Fig. 7c), with a maximum flow rate of 54 mL/s compared with 145 mL/s for tomo-PIV (62% underestimation). An increase in flow through the plane is detected compared with the rest of the cycle, but the magnitude is severely underestimated.

During filling, a large underestimation is also observed at the 75 mm depth plane (Fig. 7d) with a difference in maxima of 94 mL/s (37%) at the time of jet formation and a mean underestimation of 34 mL/s (26%) over the whole cycle. For the 50 mm depth plane, the underestimation of peak flow rate reduces to 75 mL/s (23%) (Fig. 7e), with a mean underestimation of 31 mL/s (16%) over the whole cycle. In the 25 mm plane, echo-PIV overestimates the peak velocity by 21 mL/s (11%) with a mean difference of 4 mL/s (5%) less than tomo-PIV over the whole cycle (Fig. 7f).

Velocity magnitude. Velocity magnitudes at the same depths as depicted in Figure 7a are shown in Figure 8 (average velocity in a 4 mm sphere in the center of the jet). Similarly, we see that echo-PIV underestimated the high velocities more in the planes further away from the probe. At 75 mm depth, the Root mean squared error (RMSE) of echo-PIV's velocity magnitude was 18 cm/s (17%). This underestimation reduced to 12 cm/s (12%) at 50 mm depth and 8 cm/s (12%) at 25 mm depth. RMSE for outflow was 15 cm/s (40%).

Velocity profiles, measured at the 75 mm plane (Fig. 7a, green), during jet formation and after the jet had fully formed (t1 and t2) (Fig. 8b), are shown in Figure 9. Note that echo-PIV highly underestimated the velocity profile during the early stages of filling (t1) (Fig. 9a and 9b), but correctly measured the profile a short time later (t2) (Fig. 9c and 9d). Although while the velocity magnitude was correctly measured at t2, the width of the profile is still underestimated.

SNR and PSF. Calculated SNR and PSF values are shown in Table 3. Between 25 and 75 mm depth SNR decreased by 10 dB and the lateral PSF (X and Y) increased fourfold. The PSF measured from the reconstructed tomo-PIV volumes was 0.3 mm isotropic.

DISCUSSION

Flow structures imitating the trans-mitral filling jet were produced by the LV phantom and measured in 4-D by both tomo-PIV and echo-PIV at high temporal resolution (1 kHz for imaging, 200 Hz for velocity vectors—owing to

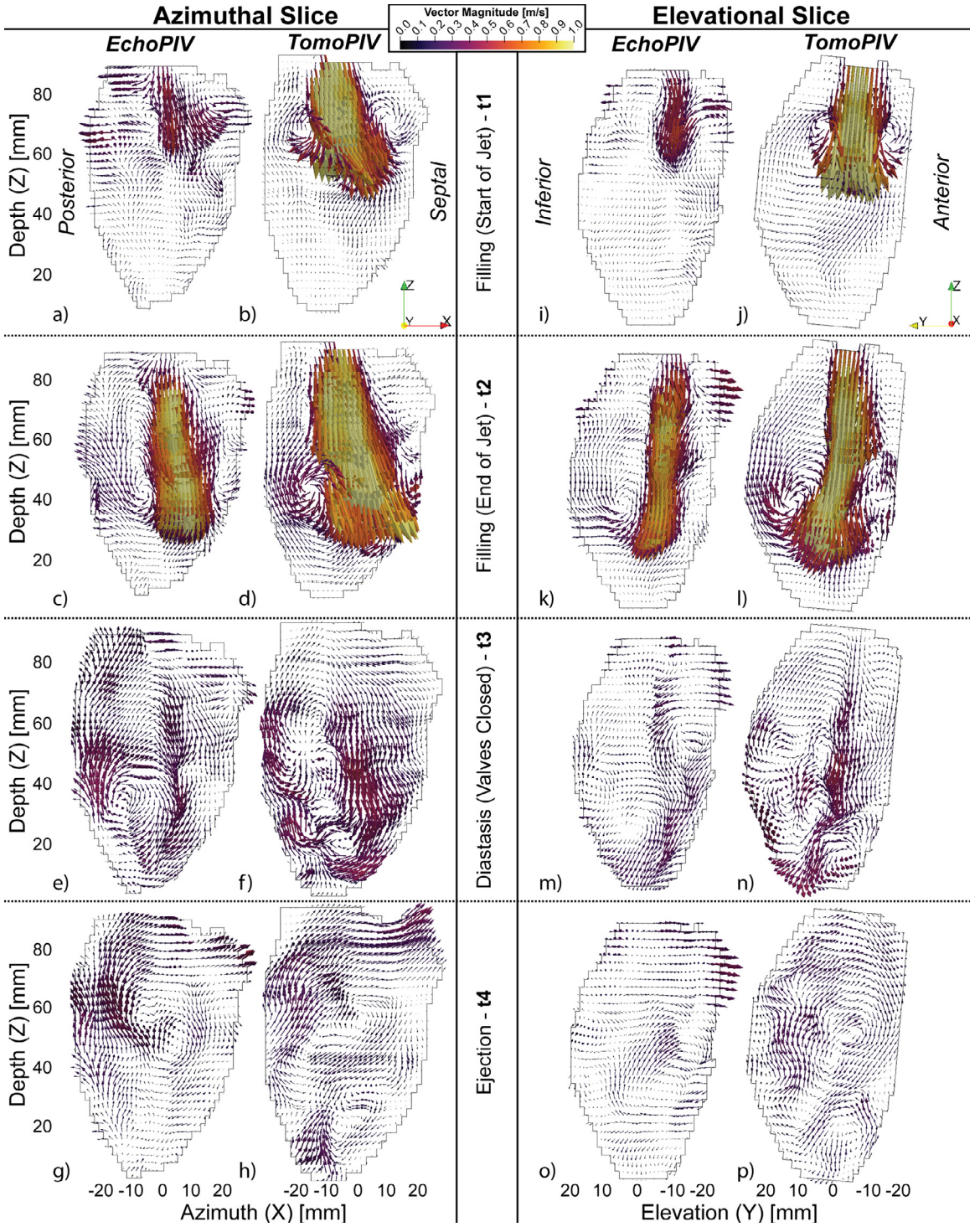

Fig. 6. (a–h) Azimuthal and (i–p) elevational slices through the center of the mitral valve at different phases of the pump cycle (t1–t4) (see Fig. 7b). See text for details. (Video S2, available online).

correlation averaging of five frames). Both techniques agreed on the general flow patterns observed, but echo-PIV underestimated the velocity magnitudes and flow rates in the deeper regions (*i.e.,* close to the mitral and aortic valves).

The two modalities agreed on the development of the central vortex on the posterior/inferior side of the LV. The part of the vortex ring on the septal and anterior sides of the LV was less defined in echo-PIV than tomo-PIV. This

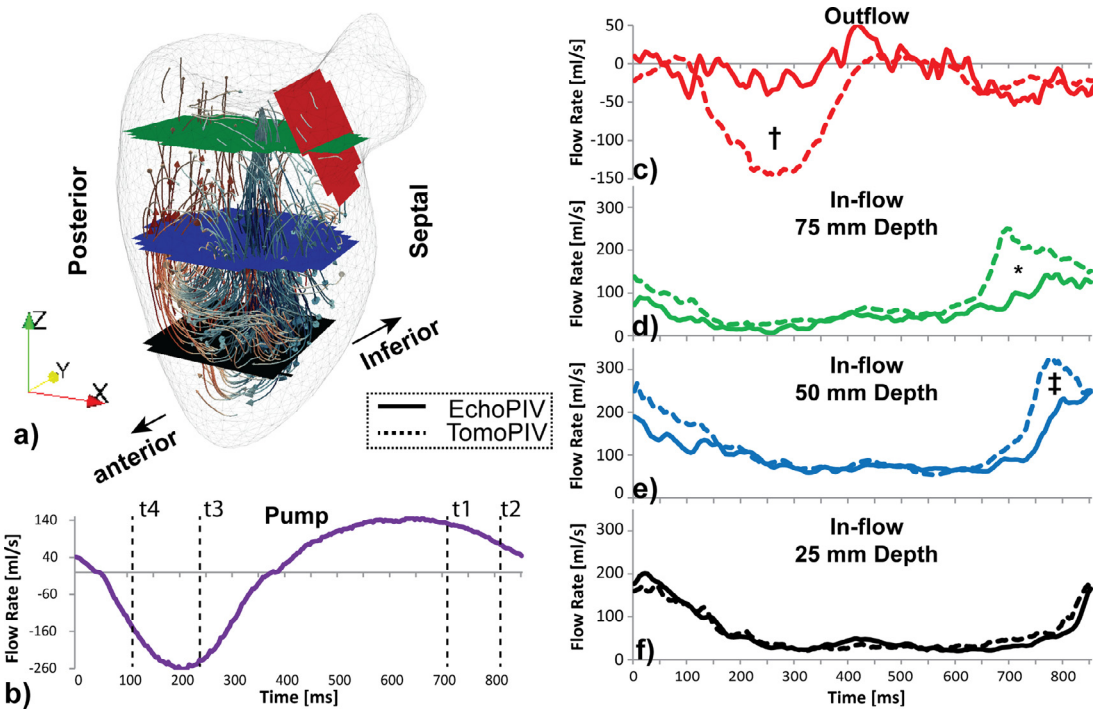

Fig. 7. (a) 3-D path-line visualization of tomo-PIV data at ~t2, with colored slices corresponding to the through-plane flow rate curves shown in (c–f). (b) Pump flow rate curve with t1–t4 indicating the time points shown in Figure 6. (c) Flow rate comparison through the outflow tract and (d–f) through horizontal planes at 75 mm (c), 50 mm (d) and 25 mm (e) depth from the transducer, limited to flow moving in the −Z direction only (inflow). Symbols *, † and ‡ refer to notable flow differences discussed in the text.

could be owing to the lateral width of the vortex on the septal/anterior side, where the lower lateral resolution of echo-PIV was not able to resolve the flow gradients.

Underestimation in jet

Echo-PIV estimated the trans-mitral jet to be of similar shape and follow the same path as tomo-PIV. However, echo-PIV largely underestimated the volume flow rate and velocity magnitudes of the jet at the start of filling (Fig. 6a vs. 6b and 6i vs. 6j). The echo-PIV estimate was more accurate closer to the probe (Fig. 6c vs. 6d and 6k vs. 6l), but the width of the jet was still estimated to be thinner than with tomo-PIV. Note that echo-PIV was able to measure similar velocity magnitudes as tomo-PIV (Fig. 9c and 9d), but estimated a thinner profile spatially and a delayed temporal response.

The increasing flow rate underestimation with distance from the probe suggests that the PSF, kernel size, SNR and/or clutter are responsible, as discussed further below.

PSF and kernel size

The kernel size used (6 mm × 5° × 5°) corresponds to approximately $6 \times 6.5 \times 6.5$ mm^3 at a distance of 75 mm from the probe, which is large relative to the final tomo-PIV kernel size (3.84^3 mm^3). The jet diameter was roughly 15 mm, and the relatively large lateral kernel size of 6.5 mm may cause averaging of the jet edges with the surrounding slow flow regions, resulting in underestimation of the jet profile that we see in Figure 9c. Note that the kernel size could not be reduced further as the lateral PSF width at that depth was ~ 4 mm after scan conversion. Note that echo-PIV's lateral PSF was ~13 times larger than that of tomo PIV at 75 mm distance from the probe. We found that using a window-refinement scheme (decreasing window size between iterations of block matching) resulted in increased underestimation and number of spurious vectors.

A similar interaction between velocity gradient and spatial resolution was found almost 30 y ago, where Foster et al. (1990) found (using pulsed wave Doppler) that longer range gates and larger beam widths increased underestimation of flow profiles with steep velocity gradients.

Wigen et al. (2018), using their 3-D hybrid autocorrelation/blood-speckle tracking estimator, reported an increasing underestimation of faster lateral velocities, but not for fast axial velocities, which were calculated using a de-aliased autocorrelation estimator. Whether the different trend in results compared to ours is caused by their larger probe aperture or by the different tracking techniques requires further studies, although it should be noted

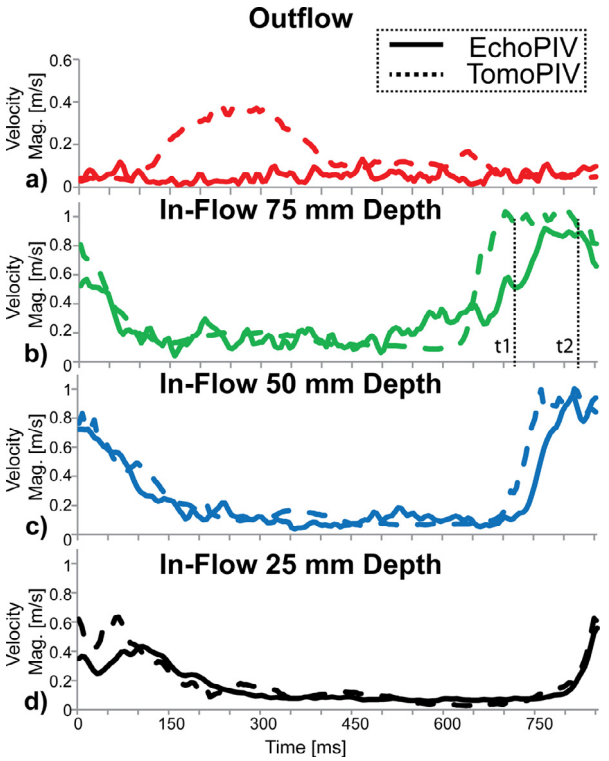

Fig. 8. Velocity magnitude comparison through a 4 mm diameter sphere in the center of the jet at different depths (the same depths as indicated in Fig. 7a). Solid/dashed lines represent the average velocity magnitude for echo-PIV and tomo-PIV. Note that echo-PIV underestimates velocities more at farther distances from the probe. Time points t1 and t2 shown again for clarity; see Figure 9 for velocity profiles these times.

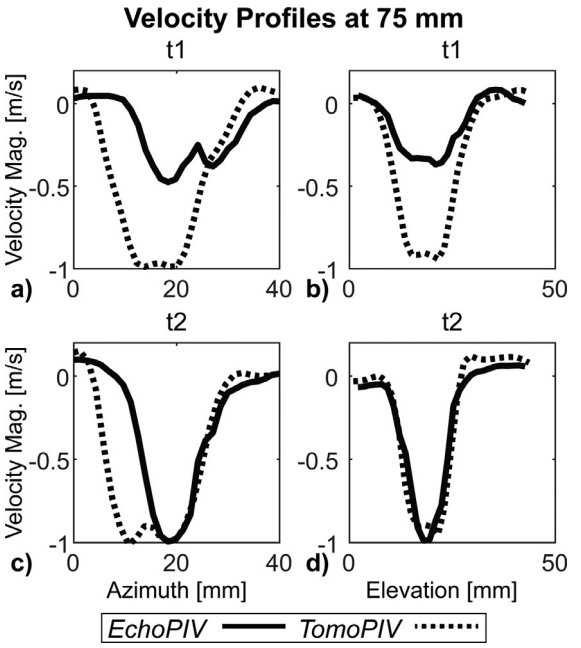

Fig. 9. Instantaneous velocity profiles, through the 75 mm plane (see Fig. 7a), at time points t1 (top row: a, b—jet formation) and t2 (bottom row: c, d—jet formed) (see Fig. 8b) along azimuthal (left column: a, c) and elevational (right column: b, d) axes. Note that echo-PIV underestimates the peak velocity profile magnitude at t1 but not at t2.

that hybrid estimators have been shown to outperform standalone block matching estimators (Tavakoli et al. 2014; Wigen and Lovstakken 2016; Poree et al. 2018).

SNR

In the case of SNR, we calculated that SNR decreased by 10 dB from 25 to 75 mm (Table 3). A study by Ekroll et al. (2018) showed that reducing SNR caused increased lateral bias in 2-D speckle tracking. However, the bias in this work was primarily axial, whereas Ekroll et al. only showed appreciable increases in axial bias at 0 dB SNR. Thus, we do not expect that SNR is the primary source of underestimation seen in the trans-mitral jet. However, SNR may play a significant role in the underestimation seen during ejection, where displacement is primarily lateral.

Clutter

Holbek et al. (2017b), when using 3-D transverse oscillation, observed a similar underestimation in flow rate and even an overestimation of peak-velocity magnitude compared with PC-MRI. They attributed the flow rate underestimation to underestimation of the velocities close to the vessel wall, where the clutter filter removed the moving blood signal. This caused "leakage" of low velocities into the blood flow profile, reducing the overall flow rate.

In this study, we tested three different Butterworth high-pass filter cutoffs (27, 55 and 110 Hz) as well as a singular value decomposition—based clutter filter with automatic low-rank truncation with the method described by Voorneveld et al. (2018a) and Yu and Lovstakken (2010).The 55 Hz high-pass Butterworth filter was used in this study because it resulted in the least amount of clutter remaining in the valve region and the least amount of underestimation in the resulting flow profiles. An adaptive clutter filter may improve the velocity results but was outside the scope of this study.

Table 3. PSF and SNR per depth

Depth (mm)	SNR (dB)	PSF (mm)		
		X	Y	Z
25	27	1.1	1.0	0.6
50	22	2.0	2.2	0.7
75	17	3.5	4.1	0.7

PSF = point spread function; SNR = signal-to-noise ratio.

Limitations

LV phantom. The flow patterns generated by the LV phantom share some key aspects with physiologic LV flows. For example, the high velocity trans-mitral jet with its accompanying vortex ring structure (Fig. 6b and 6j) and the dominant central vortex structure (Fig. 6d and 6l) which redirects the jet upward toward the base of the LV. Note that flow is not split into an early and late filling phase, as is the case physiologically. This is because the piston pump moved in a sinusoidal pattern (Fig. 7b). Interpretation of the physiologic consequences of flow patterns observed in this study should take this temporal profile into consideration. In addition, the LV shell does not include trabecular structures, nor does it contract and relax with a twisting action that is observed in the human LV (Omar et al. 2015). However, the purpose of this phantom was to create reproducible flow patterns on a scale like those observed *in vivo*, with less simplistic flow patterns than other common validation phantoms, such as the straight tube (laminar flow experiments) (Hoyos et al. 2016; Voorneveld et al. 2016) or the spinning disk phantom (Hoyos et al. 2016; Wigen and Lovstakken 2016; Faurie et al. 2017) (it should be noted that Faurie et al. [2017] and Wigen and Lovstakken [2016] also compared their techniques with PC-MRI *in vivo*). Production of these flow patterns was accomplished in a setup which can be imaged both optically and acoustically. This phantom was inspired by similar LV flow phantoms capable of both optical and acoustical imaging (Kheradvar et al. 2010; Gao et al. 2015; Asami et al. 2017), although it should be noted that in this study we utilize a more realistic LV geometry.

Imaging view. The probe used in this experiment was a TEE probe, but the imaging angle chosen is an apical transthoracic view. An apical view was used because a typical TEE view would have required the probe to be mounted on one of the walls of the LV chamber, but the walls needed to be kept clean for tomo-PIV imaging. If a more typical TEE view were used, the distance to the mitral valve area would be reduced to less than 70 mm, by viewing the LV parallel to its long axis. This shorter imaging depth would allow for a higher PRF. On the other hand, viewing the LV perpendicular to its long axis would mandate a larger lateral field of view, possibly requiring more gated acquisitions to fully sample the LV spatially.

Contrast agent. In this study, we used air bubbles as a contrast medium; *in vivo* UCA microbubbles would be used instead. Air bubbles were used because they already appeared spontaneously in the phantom's operation, and earlier iterations of the experiment indicated that addition of microbubbles did not improve the tracking result over the spontaneous air bubbles. Translation to *in vivo* applications would require the use of UCA microbubbles where studies would need to be performed to optimize microbubble concentration and acoustic pressures.

Analyses

As the tomo-PIV and echo-PIV data sets were not co-registered in space, a pair-wise analysis was not performed; thus, comparison between the flow patterns in each data set was largely qualitative. A reliable means of registering the two data sets would allow for more accurate quantitative analyses to be performed.

FUTURE PERSPECTIVES

Resolution

Improving lateral resolution is expected to reduce the spatial smoothing of the jet velocity profile and allow for smaller flow structures to be resolved. Increasing aperture size is difficult for TEE probes owing to power dissipation and spatial constraints. However, transthoracic probes have slightly more manageable power dissipation constraints, but the aperture still has to fit between the ribs $\sim$15$-$20 mm.

Alternatively using plane waves or multi-line transmit sequences may allow for better resolution at depth, which may improve accuracy. However, these imaging schemes will incur a cost in frame rate, which may complicate the clutter filtering and/or block-matching processes.

SNR

SNR at depth can be improved by transmitting at a lower frequency; however, this will result in significantly lower lateral resolution. Using pulse inversion and second harmonic filtering may help, by transmitting at 2$-$3 MHz and receiving at 4$-$6 MHz, thereby increasing penetration depth and reducing tissue clutter simultaneously.

Frame rate

The proposed acquisition sequence of four gated cycles of four beams per cycle allowed for a frame rate of 1 kHz while still scanning a field of view of $60^\circ \times 60^\circ$. The goal, of course, is for fully time-resolved 4-D velocity estimation in a single heartbeat. However, this work serves as an intermediate step, where the requirement for multiple beams was mandated by the probes micro-beamforming architecture. The PRF was limited to 4 kHz to avoid reflection artifacts from the phantom lid, which appeared in the middle of the LV at higher PRF (>5 kHz PRF should have been possible at 120 mm depth). A higher PRF would have permitted more beams per cycle, while keeping the frame rate constant, thereby reducing the number of gated cycles required for imaging the required field of view. Another method to reduce the number of gated cycles would be

to reduce the number of elements grouped together for channel reduction, because this would effectively reduce the pitch in receive so a wider beam could be formed without grating lobes.

To reduce spurious vector results, we used a correlation ensemble of five frames. Increasing the correlation ensemble length will further improve SNR in the case of low velocity gradients, but will be susceptible to correlation peak broadening in the presence of high velocity gradients. Our choice to ensemble average of five frames reduced the vector frame rate to 200 fps; however, this could also be performed using a moving average, so that the frame rate could have been preserved at 1000 fps (at the cost of computational time).

MRI

Finally, the proposed LV phantom is also MRI compatible. Future work will assess 4-D flow MRI accuracy against tomo-PIV, facilitating comparison between 4-D echo-PIV with 4-D flow MRI.

CONCLUSION

We have demonstrated, *in vitro*, that 4-D echo-PIV of the whole LV can be performed in just four heart cycles. The general flow patterns compared well with tomo-PIV, an optical technique with far superior spatial resolution. Significant underestimations in flow rates were observed in the basal region of the LV, close to the mitral and aortic valve, which were located furthest from the probe. The reason for underestimation is suspected to be owing to spatial smoothing where PSF is large relative to the spatial velocity gradients.

Acknowledgments—This work was supported in part by ZonMw within the Innovative Medical Devices Initiative program (project Heart Failure and 4-D flow). We would like to thank Franc van den Adel (Oldelft Ultrasound) for his work in designing and building the matrix probe. We acknowledge Henry den Bok (Delft University of Technology) for technical assistance with the probe setup. We also thank Geert Springeling, Michiel Manten and Robert Beurskens (Erasmus MC) for fabricating the LV phantom.

Conflict of interest disclosure—The authors declare no competing interests.

SUPPLEMENTARY MATERIALS

Supplementary material associated with this article can be found in the online version at doi:10.1016/j.ultrasmedbio.2019.11.020.

REFERENCES

Ahrens J, Geveci B, Law C. ParaView: An end-user tool for large-data visualization. In: Hansen Charles D, Johnson Chris R, (eds). Visualization Handbook. Burlington: Butterworth-Heinemann; 2005. p. 717–731. doi: 10.1016/B978-012387582-2/50038-1.

Arvidsson PM, Kovács SJ, Töger J, Borgquist R, Heiberg E, Carlsson M, Arheden H. Vortex ring behavior provides the epigenetic blueprint for the human heart. Sci Rep 2016;6:22021.

Asami R, Tanaka T, Kawabata K, Hashiba K, Okada T, Nishiyama T. Accuracy and limitations of vector flow mapping: Left ventricular phantom validation using stereo particle image velocimetory. J Echocardiogr 2017;15:57–66.

Assi KC, Gay E, Chnafa C, Mendez S, Nicoud F, Abascal JFPJ, Lantelme P, Tournoux F, Garcia D. Intraventricular vector flow mapping - A Doppler-based regularized problem with automatic model selection. Phys Med Biol 2017;62:7131–7147.

Bera D, van den Adel F, Radeljic-Jakic N, Lippe B, Soozande M, Pertijs MAP, Verweij MD, Kruizinga P, Daeichin V, Vos HJ, van der Steen AFW, Bosch JG, de Jong N. Fast Volumetric imaging using a matrix transesophageal echocardiography probe with partitioned transmit−receive array. Ultrasound Med Biol 2018;44:2025–2042.

Correia M, Provost J, Tanter M, Pernot M. 4D ultrafast ultrasound flow imaging: I*n vivo* quantification of arterial volumetric flow rate in a single heartbeat. Phys Med Biol 2016;61:L48–L61.

Dyverfeldt P, Bissell M, Barker AJ, Bolger AF, Carlhäll CJ, Ebbers T, Francios CJ, Frydrychowicz A, Geiger J, Giese D, Hope MD, Kilner PJ, Kozerke S, Myerson S, Neubauer S, Wieben O, Markl M. 4 D flow cardiovascular magnetic resonance consensus statement. J Cardiovasc Magn Reson 2015;17:1–19.

Ekroll IK, Wigen M, Fadnes S, Adval J. Quantitative vascular blood flow imaging: a comparison of vector velocity estimation schemes. IEEE International Ultrasonics Symposium (IUS) 2018;1–4. doi: 10.1109/ULTSYM.2018.8579692.

Fadnes S, Wigen MS, Nyrnes SA, Lovstakken L. In vivo intracardiac vector flow imaging using phased array transducers for pediatric cardiology. IEEE Trans Ultrason Ferroelectr Freq Control 2017; 64:1318–1326.

Faurie J, Baudet M, Assi KC, Auger D, Gilbert G, Tournoux F, Garcia D. Intracardiac vortex dynamics by high-frame-rate doppler vortography-in vivo comparison with vector flow mapping and 4-D flow MRI. IEEE Trans Ultrason Ferroelectr Freq Control 2017;64:424–432.

Foster SG, Embree PM, O'Brien WD. Flow velocity profile via time-domain correlation: Error analysis and computer simulation. IEEE Trans Ultrason Ferroelectr Freq Control 1990;37:164–175.

Gao H, Bijnens N, Coisne D, Lugiez M, Rutten M, D'hooge J. 2-D left ventricular flow estimation by combining speckle tracking with Navier−Stokes-based regularization: An in silico, in vitro and in vivo study. Ultrasound Med Biol 2015;41:99–113.

Gao H, Heyde B, D'hooge J. 3 D Intra-cardiac flow estimation using speckle tracking: A feasibility study in synthetic ultrasound data. IEEE Int Ultrason Symp 2013;68–71.

Garcia D, del Álamo JC, Tanné D, Yotti R, Cortina C, Bertrand É, Antoranz JC, Pérez-David E, Rieu R, Fernández-Avilés F, Bermejo J. Two-dimensional intraventricular flow mapping by digital processing conventional color-Doppler echocardiography images. IEEE Trans Med Imaging 2010;29:1701–1713.

Gomez A, De Vecchi A, Jantsch M, Shi W, Pushparajah K, Simpson J, Smith N, Rueckert D, Schaeffter T, Penney G. 4 D blood flow reconstruction over the entire ventricle from wall motion and blood velocity derived from ultrasound data. IEEE Trans Med Imaging 2015;34:2298–2308.

Grønli T, Wigen M, Segers P, Lovstakken L. A fast 4 D B-spline framework for model-based reconstruction and regularization in vector flow imaging. IEEE Int Ultrason Symp IUS 2018;1:2–5.

Holbek S, Ewertsen C, Bouzari H, Pihl MJ, Hansen KL, Stuart MB, Thomsen C, Nielsen MB, Jensen JA. Ultrasonic 3-D vector flow method for quantitative in vivo peak velocity and flow rate estimation. IEEE Trans Ultrason Ferroelectr Freq Control 2017; 64:544–554.

Holbek S, Hansen KL, Bouzari H, Ewertsen C, Stuart MB, Thomsen C, Nielsen MB, Jensen JA. Common carotid artery flow measured by 3-D ultrasonic vector flow imaging and validated with magnetic resonance imaging. Ultrasound Med Biol 2017;43:2213–2220.

Hoyos CAV, Stuart MB, Hansen KL, Nielsen MB, Jensen JA. Accurate angle estimator for high-frame-rate 2-D vector flow imaging. IEEE Trans Ultrason Ferroelectr Freq Control 2016;63:842–853.

Kheradvar A, Assadi R, Falahatpisheh A, Sengupta PP. Assessment of transmitral vortex formation in patients with diastolic dysfunction. J Am Soc Echocardiogr 2012;25:220–227.

Kheradvar A, Houle H, Pedrizzetti G, Tonti G, Belcik T, Ashraf M, Lindner JR, Gharib M, Sahn D. Echocardiographic particle image velocimetry: a novel technique for quantification of left ventricular blood vorticity pattern. J Am Soc Echocardiogr 2010;23: 86–94.

Kirişli HA, Schaap M, Klein S, Papadopoulou SL, Bonardi M, Chen CH, Weustink AC, Mollet NR, Vonken EJ, van der Geest RJ, van Walsum T, Niessen WJ. Evaluation of a multi-atlas based method for segmentation of cardiac CTA data: A large-scale, multicenter, and multivendor study. Med Phys 2010;37:6279–6291.

Lai X, Torp H, Kristoffersen K. An extended autocorrelation method for estimation of blood velocity. IEEE Trans Ultrason Ferroelectr Freq Control 1997;44:1332–1342.

Martínez-Legazpi P, Bermejo J, Benito Y, Yotti R, Pérez del Villar C, González-Mansilla A, Barrio A, Villacorta E, Sánchez PL, Fernández-Avilés F, del Álamo JC. Contribution of the diastolic vortex ring to left ventricular filling. J Am Coll Cardiol 2014; 64:1711–1721.

Metz CT, Baka N, Kirisli H, Schaap M, Klein S, Neefjes LA, Mollet NR, Lelieveldt B, de Bruijne M, Niessen WJ, van Walsum T. Regression-based cardiac motion prediction from single-phase CTA. IEEE Trans Med Imaging 2012;31:1311–1325.

Muth S, Dort S, Sebag IA, Blais M-J, Garcia D. Unsupervised dealiasing and denoising of color-Doppler data. Med Image Anal 2011; 15:577–588.

Omar AMS, Vallabhajosyula S, Sengupta PP. Left ventricular twist and torsion. Circ Cardiovasc Imaging 2015;8:74–82.

Pasipoularides A. Mechanotransduction mechanisms for intraventricular diastolic vortex forces and myocardial deformations: Part 1. J Cardiovasc Transl Res 2015;8:293–318.

Pedrizzetti G, Martiniello AR, Bianchi V, D'Onofrio A, Caso P, Tonti G. Cardiac fluid dynamics anticipates heart adaptation. J Biomech 2015;48:388–391.

Poelma C, Mari JM, Foin N, Tang M-X, Krams R, Caro CG, Weinberg PD, Westerweel J. 3 D flow reconstruction using ultrasound PIV. Exp Fluids 2011;50:777–785.

Poree J, Baudet M, Tournoux F, Cloutier G, Garcia D. A Dual Tissue-Doppler optical-flow method for speckle tracking echocardiography at high frame rate. IEEE Trans Med Imaging 2018;37: 2022–2032.

Posada D, Poree J, Pellissier A, Chayer B, Tournoux F, Cloutier G, Garcia D. Staggered multiple-PRF ultrafast color Doppler. IEEE Trans Med Imaging 2016;35:1510–1521.

Saaid H, Voorneveld J, Schinkel C, Westenberg J, Gijsen F, Segers P, Verdonck P, de Jong N, Bosch JG, Kenjeres S, Claessens T. Tomographic PIV in a model of the left ventricle: 3 D flow past biological and mechanical heart valves. J Biomech 2019;90:40–49.

Scarano F, Riethmuller ML. Advances in iterative multigrid PIV image processing. Exp Fluids 2000;29:S051–S060.

Sengupta PP, Pedrizetti G, Narula J. Multiplanar visualization of blood flow using echocardiographic particle imaging velocimetry. JACC Cardiovasc Imaging 2012;5:566–569.

Sengupta PP, Pedrizzetti G, Kilner PJ, Kheradvar A, Ebbers T, Tonti G, Fraser AG, Narula J. Emerging trends in CV flow visualization. JACC Cardiovasc Imaging 2012;5:305–316.

Tavakoli V, Bhatia N, Longaker RA, Stoddard MF, Amini AA. Tissue Doppler imaging optical flow (TDIOF): A combined b-mode and tissue Doppler approach for cardiac motion estimation in echocardiographic images. IEEE Trans Biomed Eng 2014;61:2264–2277.

Toulemonde MEG, Corbett R, Papadopoulou V, Chahal N, Li Y, Leow CH, Cosgrove DO, Eckersley RJ, Duncan N, Senior R, Tang MX. High frame-rate contrast echocardiography: In-human demonstration. JACC Cardiovasc Imaging 2018;11:923–924.

Voorneveld J, Kruizinga P, Vos HJ, Gijsen FJH, Jebbink EG, van der Steen AFW, de Jong N, Bosch JG. Native blood speckle vs ultrasound contrast agent for particle image velocimetry with ultrafast ultrasound - in vitro experiments. IEEE Int Ultrason Symp 2016;1–4.

Voorneveld J, Engelhard S, Vos HJ, Reijnen MMPJ, Gijsen F, Versluis M, Jebbink EG, de Jong N, Bosch JG. High frame rate contrast-enhanced ultrasound for velocimetry in the human abdominal aorta. IEEE Trans Ultrason Ferroelectr Freq Control 2018;65:2245–2254.

Voorneveld J, Muralidharan A, Hope T, Vos HJ, Kruizinga P, van der Steen AFW, Gijsen FJH, Kenjeres S, de Jong N, Bosch JG. High frame rate ultrasound particle image velocimetry for estimating high velocity flow patterns in the left ventricle. IEEE Trans Ultrason Ferroelectr Freq Control 2018;65:2222–2232.

Voorneveld J, Keijzer LBH, Strachinaru M, Bowen DJ, Goei JSL, Ten Cate F, van der Steen AFW, de Jong N, Vos HJ, van den Bosch AE, Bosch JG. High-frame-rate echo-particle image velocimetry can measure the high-velocity diastolic flow patterns. Circ Cardiovasc Imaging 2019;12 e008856.

Westerweel J, Scarano F. Universal outlier detection for PIV data. Exp Fluids 2005;39:1096–1100.

Wigen M, Lovstakken L. In vivo three-dimensional intra-cardiac vector flow imaging using a 2 D matrix array transducer. IEEE Int Ultrason Symp 2016;2–5.

Wigen MS, Fadnes S, Rodriguez-Molares A, Bjastad T, Eriksen M, Stensaeth KH, Stoylen A, Lovstakken L. 4 D Intracardiac ultrasound vector flow imaging-feasibility and comparison to phase-contrast MRI. IEEE Trans Med Imaging 2018;37:2619–2629.

Yu A, Lovstakken L. Eigen-based clutter filter design for ultrasound color flow imaging: A review. IEEE Trans Ultrason Ferroelectr Freq Control 2010;57:1096–1111.

Zhou X, Leow CH, Rowland E, Riemer K, Rubin JM, Weinberg PD, Tang M. 3 D velocity and volume flow measurement in vivo using speckle decorrelation and 2 D high frame rate contrast-enhanced ultrasound. IEEE Trans Ultrason Ferroelectr Freq Control 2018;1–11.

Zhou X, Papadopoulou V, Leow CH, Vincent P, Tang MX. 3-D flow reconstruction using divergence-free interpolation of multiple 2-D contrast-enhanced ultrasound particle imaging velocimetry measurements. Ultrasound Med Biol 2019;45:795–810.

Zhou X, Vincent P, Zhou X, Leow CH, Tang M-X. Optimization of 3-D divergence-free flow field reconstruction using 2-D ultrasound vector flow imaging. Ultrasound Med Biol 2019;45:3042–3055.

Zhou X, Zhou X, Leow CH, Tang M-X. Measurement of flow volume in the presence of reverse flow with ultrasound speckle decorrelation. Ultrasound Med Biol 2019;45:3056–3066.